High-throughput analysis of membrane order unveils a hidden dimension in immune cell states

Luca A. Andronico[1,2,*], Cenk O. Gurdap[1,2], Abishek Arora[1,2], Patrick A. Sandoz[1,3,4], Yidan Jiang[1,2,5], Sarantis Giatrellis[5], Leon de Boer[1], Valentina Carannante[1,3], Sofiia Iskrak[1,2], Jaromir Mikes[2], Marcus Buggert[7], Anders Österborg[8,9], Björn Önfelt[1,3,7], Andrey Klymchenko[10], Petter Brodin[2,11,12] & Erdinc Sezgin[1,2*]

[1] Science for Life Laboratory, 171 65 Solna, Sweden.
[2] Department of Women's and Children's Health, Karolinska Institutet, 17165 Solna, Sweden.
[3] Department of Applied Physics, KTH Royal Institute of Technology, 114 28 Stockholm, Sweden.
[4] Department of Materials Science and Engineering, Uppsala University, 751 03, Uppsala, Sweden.
[5] European Molecular Biology Laboratory (EMBL), 69117, Heidelberg, Germany.
[6] Department of Cell and Molecular Biology, Karolinska Institute; 171 77 Stockholm, Sweden.
[7] Department of Medicine Huddinge, Centre for Infectious Medicine, Karolinska Institutet, 171 77, Stockholm, Sweden.
[8] Department of Hematology, Karolinska University Hospital, Stockholm, Sweden.
[9] Department of Oncology-Pathology, Karolinska Institutet, 171 77, Stockholm, Sweden.
[10] Laboratoire de Bioimagerie et Pathologies, UMR 7021 CNRS, Université de Strasbourg 74 Route du Rhin 67401 Illkirch France.
[11]Medical Research Council Laboratory of Medical Sciences (MRC LMS), Imperial College Hammersmith Campus, London, UK.
[12]Department of Immunology and Inflammation, Imperial College London, W12 0NN, London, UK.

Correspondence:

Erdinc Sezgin

erdinc.sezgin@ki.se

0046702318248

Luca Andronico

luca.andronico@ki.se

0046730653543

Abstract

Cell membranes undergo biophysical remodelling as an adaptation to the surroundings and to perform specific biological functions. However, the extent and relevance of such changes in human immune cells remain unknown, largely due to the lack of high throughput and multidimensional methodologies. Here, we describe a cytometry-based method with single-cell resolution which fills this gap by combining biophysical profiling with simultaneous analysis of multiple immune cell markers. This platform allows to reveal notable cell type-dependent remodelling of plasma membrane order in diseases. By sorting immune cells based on their membrane order and performing functional and transcriptomic analyses, we link the plasma membrane order with cell states and reveal the underling transcriptomic codes. Our findings demonstrate a broad heterogeneity of plasma membrane order in immune cells that will provide a more precise definition of immune cell states based on their biophysical properties in health and disease.

Keywords: plasma membrane order, flow cytometry, immunophenotyping, transcriptomics, inflammation, long COVID, chronic lymphocyte leukaemia

Introduction

Immune cells are dynamically regulated across tissues, over the course of life and in relation to stimulation, offering spatiotemporal control of immunity. Recent data suggests a continuum of archetypal cell states as a key component of immune system heterogeneity[1]. This concept proposes that cells can assume various states depending on their microenvironment and stimulants therein[2]. While cell types are mostly defined by surface markers or transcriptional regulation and hence can be robustly distinguished[3], cell state definitions are more complex, and requires multiparametric analysis of macromolecular content.

Lipids are fundamental to maintaining cell homeostasis as they allow for energy storage via lipid droplets formation[4], organelle compartmentalization, by self-organizing in membranes[5,6], and intracellular signalling by acting as secondary messengers[7]. Lipids exert their function by operating as a complex dynamic system of hundreds of molecules interacting with one another. This is evident in cell membranes, where the collective interaction between different lipid species dictates properties of the plasma membrane (PM) such as polarity, order (also referred to as membrane fluidity), viscosity, bending rigidity etc[8,9]. These biophysical properties have been shown to change during cellular processes such as proliferation and migration[10–14]. More recently, evidence has started highlighting the relationship between membrane biophysical properties and immune cell activity[15–23]. Importantly, alterations in cellular biophysical properties could occur without any changes in the genomic and transcriptomic profiles of dysfunctional cells (e.g., induced by nutrients or immediate microenvironment)[24,25], which makes them complementary cell state indicators.

Cellular biophysical properties are commonly investigated by means of environment-sensitive fluorescent probes, whose photophysical properties change upon physical/chemical changes in the environment[26–31]. In particular, solvatochromic dyes, such as Laurdan, Nile Red and their derivatives, which shift their emission spectra as a function of local polarity and hydration, reflecting lipid order in biomembranes are widely used[32]. However, the use of such probes remains largely confined to microscopy techniques[33], with only a few examples of their application in high-throughput methodologies such as flow cytometry. For instance, flow cytometry combined with environment-sensitive probes has been used to measure PM order in cell lines[34] and bacteria[35–37]. Similar approaches have been applied to characterize PM order remodelling in immune cells. Miguel et al., for instance, focused on $CD4^+$ T cells, comparing PM order differences between healthy donors and patients with autoimmune rheumatic disease[38], demonstrating a strong correlation between membrane order and cell functionality. These studies focused on a specific cell type; however, capturing the broader heterogeneity in biophysical properties across major immune cell populations requires measuring many immune cell types simultaneously. Here, we take on this challenge by expanding the characterization of PM order across multiple immune cell types simultaneously. We achieve this by combining flow cytometry with a recently developed narrow-emission, plasma membrane-specific solvatochromic probe, Pro12A[39], which enables correlative analysis of cell biophysical properties (Fig. S1). Furthermore, we establish a link between PM order remodeling and specific cell phenotype and function. Our findings demonstrate that biophysical properties represent an underexplored dimension in cell phenotyping, with the potential to enhance diagnostic capabilities and improve our understanding of cellular (dys)functional states.

Results

Plasma membrane order is highly heterogeneous among immune cells. To investigate the extent of PM order heterogeneity in health and disease, we first compared the PM order in primary Peripheral Blood Mononuclear Cells (PBMCs) isolated from healthy donors (HD; 15 donors) and patients affected by chronic inflammation, namely Chronic Lymphocytic Leukemia (CLL; 5 donors) and Post-Acute Sequelae of COVID-19 infection (long COVID, LC; 15 donors) (Fig. 1A). After optimizing protocols for sample preparation[40] and flow cytometry settings, we maximized the sensitivity of Pro12A in detecting minute differences in PM order across a wide range of membrane compositions while ensuring its compatibility with live-cell analysis (Fig. S2-S3). Next, we designed a panel of cell surface markers to identify cell lineages that was compatible with our probe for PM order (i.e., minimal spectral overlap) and enabled us to identify 12 different immune cell subsets and PM order measurements using Pro12A (Fig. S4). The intensities of Pro12A, measured in two different channels, were used to calculate PM order—as Normalized Generalized Polarization (ΔGP)—for individual cells (Eq. S1-S2) where higher ΔGP values represent higher membrane order.

Comparing the whole PBMC populations between healthy donors and patients (Fig. 1B-C), we observed a systematic rigidification of the plasma membrane (i.e., higher ΔGP) in long COVID patients but not in those affected by CLL. This suggests a different remodelling of PM order depending on whether the insult is a viral infection or a tumour[41–46]. Using Uniform Manifold Approximation and Projection (UMAP), we clustered the 12 different immune cell subtypes and characterized the inter-population heterogeneity of ΔGP (Fig. 1D). A closer examination of individual immune cell subpopulations revealed different cell type specific distributions of ΔGP values. For instance, in PBMCs from healthy donors (Fig. 1E), Cytotoxic T cells and NK cells exhibited a primarily monomodal distribution, whereas Monocyte-derived Dendritic cells (Mo-DCs) and B cells followed a multimodal distribution of ΔGP values with changes in relative abundances. These findings highlight the importance of examining the distribution of ΔGP values for multiple cell types simultaneously to capture the fine details in cell type-specific biophysical remodelling, which would be lost if we focused exclusively on descriptive parameters (means and medians) and a single cell type.

Across all cell types and samples, we observed a broad and continuous ΔGP distribution, which was categorized into three main populations: a high-ΔGP population centred at ~0.8 ΔGP (high-ΔGP), and two smaller populations with significantly lower PM order, centred at ~0.30 (low-ΔGP) and ~0.55 ΔGP (int-ΔGP), respectively (Fig. 1E, bottom-right panel). The left-most population (low-ΔGP) exhibited ΔGP values typical of dead cells (Fig. S5). Upon cell death, the plasma membrane becomes highly permeable, allowing Pro12A to internalize and stain intracellular organelle membranes, which have much lower order due to their specific lipid composition[9,47]. Thus, the low-ΔGP subset represents apoptotic cells with compromised plasma membrane integrity (Fig. S5).

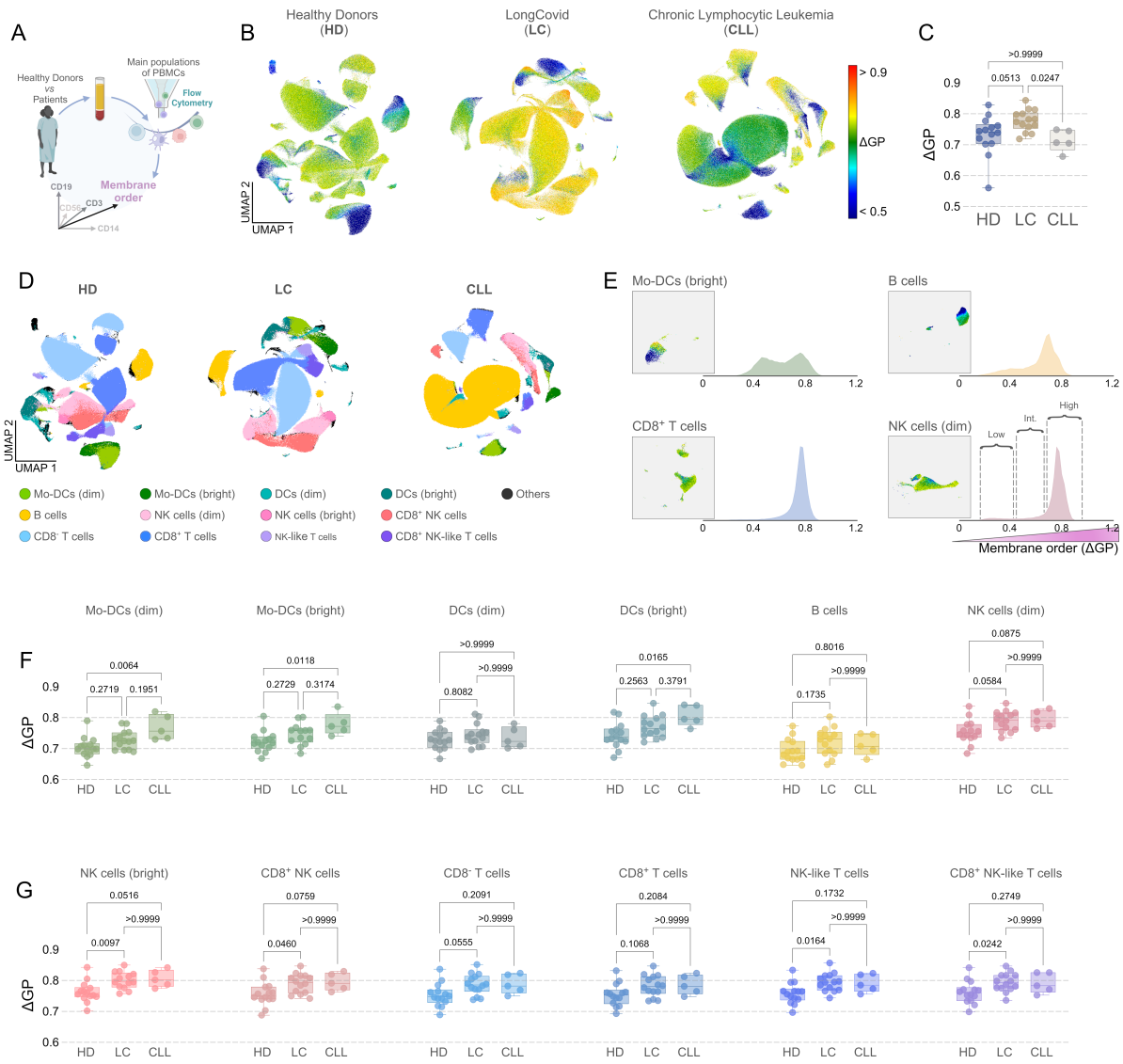

Figure 1. A) Schematic of the flow pipeline for measuring of membrane order (ΔGP) in healthy and diseased PBMCs. **B)** UMAP projections obtained from healthy and diseased PBMCs which show the distribution of membrane order values across immune cells. Pseudo colours indicate variations in ΔGP between 0.5–1. **C)** Box plots comparing the overall median ΔGP value of whole PBMCs from healthy donors and patients with long COVID and Chronic Lymphocytic Leukaemia. Each dot refers to a different donor. **D)** UMAP projections obtained from healthy and diseased PBMCs, showing the distribution of immune cell types across healthy and diseased samples. Pseudo colours indicate the different subpopulation of immune cells analysed. **E)** Pooled ΔGP distributions from selected subpopulation of immune cells from four healthy donors. The insets show to the corresponding populations in the UMAP projection whereas the dashed lines mark three distinct populations of cells with different PM order. **F-G)** Box plots comparing the ΔGP values (only for high-ΔGP population) between healthy and diseased donors for a given subpopulation of immune cells. Each dot refers to a different donor. In C, F and G, the small number represent the *p*-values calculated via the Kruskal-Wallis statistical test and the Dunn's test for multiple comparison. The threshold for statistical significance was set at $p = 0.05$.

Comparing single-donor ΔGP of the high-ΔGP population for each immune cell subpopulation, we observed general trends: Mo-DCs and Dendritic cells showed a systematic increase in PM order moving from healthy donors to LC and CLL patients. Notably, no statistical difference was observed when comparing ΔGP values in DCs (dim) and B cells. PM order in NK and T cell subsets was higher in LC and CLL patients compared to healthy donors but similar between the two patient groups. Interestingly, some cell subtypes exhibited an opposite trend

for the int-ΔGP population as seen in DCs and NK cells (Fig. S5B-C) which led us to investigate this population in detail.

Cells with intermediate PM order (int-GP) represent a distinct biophysical state. While low-GP represents late apoptotic cells, int-GP pool needs in detail analysis as it shows intriguing trends in diseased cells (Fig. S5). Therefore, we investigated whether the remodelling of PM order in the int-ΔGP population is a reflection of poor cellular health or a specific cell state. First, we observed that the int-ΔGP population was primarily enriched in $CD14^+$ cells (monocytes and monocyte-derived DCs) and, to a lesser extent, in B cells (Fig. S5). The enrichment was consistent across both healthy donors and patients with chronic inflammation. This suggests that certain immune cell subsets are inherently more heterogenous in PM order regardless of donor's health status. Next, we examined cellular health in cells within the int-ΔGP gate by co-staining PBMCs from four healthy donors with fluorescently labelled Annexin-V (AnV) and a viability marker which are used to detect apoptotic cells. During apoptosis, phosphatidylserine (PS) accumulates in the outer leaflet of the plasma membrane[48], leading to an overall shift in PM order and enabling Annexin-V binding[34]. More recently, studies have suggested broader implications of PS exposure, demonstrating its occurrence in other processes other than cell death[49–51]. Therefore, a viability dye is used for detecting cell death. It is internalized in cells where the membrane integrity is compromised, hence dead cells are positive for this marker.

By using these two markers, we analysed the PM order of AnV-negative (*neg-AnV*, no signal for AnV and viability dye), viable AnV-positive (v-pos-AnV, positive signal for AnV but no signal for viability dye), and non-viable AnnexinV-positive (nv-pos-AnV, positive signal for both AnV and viability dye) via flow cytometry (Fig. 2A-B, Fig. S6). We confirmed the presence of three populations, characterized by low, intermediate and high PM order that predominantly correspond to nv-pos-An, v-pos-An and neg-AnV, respectively. However, int-GP cells were present both in neg-AnV and v-pos-AnV cells (Fig. 2B, Fig. S6), indicating a pool of cells with lower membrane order within healthy cells.

To assess whether the decrease in ΔGP was due to a reduction in PM order or partial internalization of Pro12A, we used spectral confocal microscopy which supported our flow cytometry observations (Fig. 2C) and confirmed the existence of three distinct cell populations and found no evidence of Pro12A internalization in cells with int-ΔGP. These cells displayed a punctate accumulation of AnV. A similar pattern has been reported in T cells upon receptor-mediated activation and attributed to localized membrane scrambling leading to PS exposure[50]. When we profiled lipid order along the membrane, we observed a global reduction in ΔGP, not just at the AnV clustering sites (Fig. S7, S8). This suggests that membrane order remodelling is more global than localized to PS^+ spots which could be caused by partial breakage of membrane asymmetry[52] but not the membrane integrity. Altogether, our findings shows that int-ΔGP pool is not apoptotic cells (at least as tested with AnV) and instead corresponds to viable cells with a different biophysical state than high-ΔGP pool, positioning PM order as a potential new dimension in immune cell phenotyping.

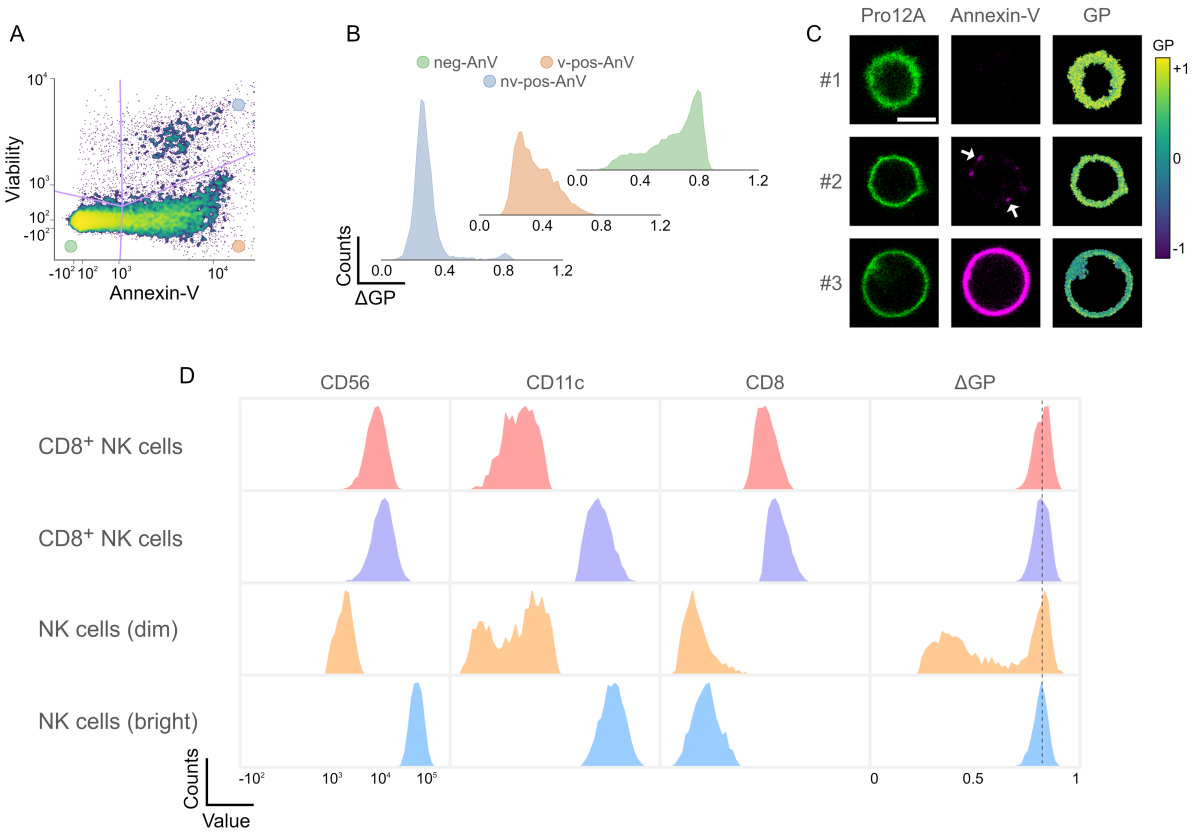

Figure 2. A) Intensity plot from cells stained with dyes for both cell viability (FVS780) and PS (Annexin-V-AF647) analysed in flow cytometry. The plot refers to T cells ($CD3^+$) from healthy donors. **B)** ΔGP distributions of healthy (neg-AnV), viable AnV-positive (v-pos-AnV), and non-viable AnV-positive T cells from one of four healthy donors. **C)** Microscopy images acquired with a spectral confocal microscope, showing three different cells (#1, #2 and #3) after being stained with both Pro12A and Annexin-V-AF647. Green, magenta and pseudo-coloured images refer to Pro12A, AnV and calculated GP values, respectively. The scale bar indicates 5 µm distance and the white arrows indicate AnV puncta. **D)** Histograms showing the intensity distribution of different biomarkers and the distribution of ΔGP values (far right column) for each subpopulation of NK cells from long COVID patients.

Plasma membrane order is an orthogonal parameter to canonical cell surface markers. After exploring that ΔGP can be an indication of disease (Fig. 1) and high-ΔGP and int-ΔGP pools might represent different cell states (Fig 2A-C), we asked whether ΔGP can be correlated with surface biomarkers, which are commonly used to identify cell types, states and diseases. Notably, we found orthogonality between ΔGP and most cell biomarkers, with their correlation (either positive or negative) depending on the cell type and sample under examination (Fig. 2D, Fig. S9–S12). For instance, when we compared PM order in $CD8^+$ NK cells, we observed that cells with higher PM order have the same level of CD56 and CD8 but lower CD11c signal (Fig. 2D, upper two rows). In contrast, for NK cells with low CD56 expression (NK cells (dim)), lower CD11c expressing cells showed lower GP and a notable pool of int-ΔGP. In comparison, NK cells with high CD56 expression (NK cells (high)) showed higher CD11c expression and higher GP values with no notable int-ΔGP population (Figure 2D, lower two rows, Fig. S12). Our findings show that PM order remodelling may be associated with different cell states and could potentially define previously unidentified immune cell subsets with complex surface signature (as seen in Fig. 2 with three differentially expressed markers on the surface). Considering the complexity of the surface marker signature and its correlation with cellular fitness; PM order will be an easy and straightforward way to access functionally different cell states. Therefore, we set out to investigate the functionality of NK cells with different membrane order and whether we can predict cellular fitness via PM order.

Lower PM order correlates with faster migration of NK cells. Having observed the link between PM order and the expression of surface biomarkers, we next tested whether ΔGP could be used to isolate immune cells with distinct functional states and properties. For this, we sorted NK cells solely based on their PM order and performed functional assays on NK cell subsets characterized by either low (NK-L) or high (NK-H) PM order. The killing efficiency of NK cells depends on their ability to migrate towards and physically engage the target cells, followed by the induction of cell death. Therefore, we tested both the migration and the killing efficiency of NK cells as a function of their PM order.

We began by enriching NK cells from whole PBMCs isolated from multiple donors and performed biophysical sorting of these cells. Specifically, we collected cells whose PM order fell below the 15th percentile (NK-L) and above the 85th percentile (NK-H) of the total ΔGP distribution after excluding the apoptotic cells (Fig. 3A, Methods for details). Sorted cells were cultured in recovery medium for 24 hours prior to functional assays. For the chemotaxis assays to assess potential differences in migration, NK-L and NK-H cells were seeded on ICAM-1–coated coverslips and exposed to a CXCL12 chemokine gradient (Fig. 3B). Analysis of migration trajectories (Fig. 3C) revealed that NK-L cells —characterized by a more fluid plasma membrane— migrated significantly faster than NK-H cells (Fig. 3D). Despite high inter-donor variability, each donor exhibited a consistent trend, with NK-L cells migrating approximately 25% faster on average. Several mechanisms may underlie this observation, since PM order can directly or indirectly influence cell migration at multiple levels. To reveal whether the PM order is directly involved in migration capacity, we measured the PM order after recovery and observed that the difference in ΔGP between the two populations normalized after 24h of recovery in culture conditions, converging to an intermediate value (Fig. S13). This suggests that PM order at the time of selection is an indicator but not a direct determinant of the migration of NK cells at the time of measurements, which will be discussed later.

NK cells with increased PM order show higher killing efficiency. We continued our functional characterization of biophysically sorted NK cells by performing killing assays (Fig. 3E). After 24 hours of recovery in cell culture medium, NK-H and NK-L cells were each mixed with an equal number of K562 tumour cells and incubated for 6 hours. Subsequently, cells were stained with a cocktail of antibodies, including a viability dye and CD107a—a marker of degranulation of NK cells—and analysed by flow cytometry. The cytotoxic efficacy of NK cells was assessed using two independent approaches: *(i)* by calculating the ratio of live NK-H cells to NK-L cells (NK-H/NK-L) with the ratio between live tumour cells from the two subsets (i.e., T(H)/T(L)), and *(ii)* by measuring CD107a expression levels. CD107a upregulation at the cell surface indicates the extent of degranulation[53] while the ratio of live NK-H/NK-L cells and T(H)/T(L) reflect the effectiveness of degranulation and NK cell resilience to self-killing. Live tumour cells were identified based on light scatter characteristics (Fig. 3F), while live NK cells were gated as CD56-positive and viability dye-negative (Fig. S13). Looking at the ratios of live tumour cells and live NK cells between the NK-H and NK-L subsets (Fig. 3G), cells with higher PM order killed ~10% more tumour cells and maintained approximately 24% higher viability compared to NK-L cells. The moderate increase in number of killed targets could be because sorted NK cells did not undergo any interleukin-based activation prior to incubation with tumours. Furthermore, NK cells with higher PM order showed a 27% increase in the frequency of degranulating cells (Fig. 3H-J, Fig. 13) and a 34% higher CD107a signal intensity on average (Fig. 3K, Fig. S13). Collectively, our results suggest that while the actual killing efficiency was moderately better in our experimental setup, NK-H cells can potentially be better killers due to both enhanced survival after degranulation and more effective release of lytic granules. Since we previously observed that PM order converges in NK-L and NK-H pools during recovery in culture conditions, it is likely that we selected different functional cell states by biophysical sorting; and PM order is an indicator of cell states but not a direct determinant

for killing. Therefore, for the cell state identification of NK-L vs. NK-H pools, we next performed transcriptomics analysis of sorted pools.

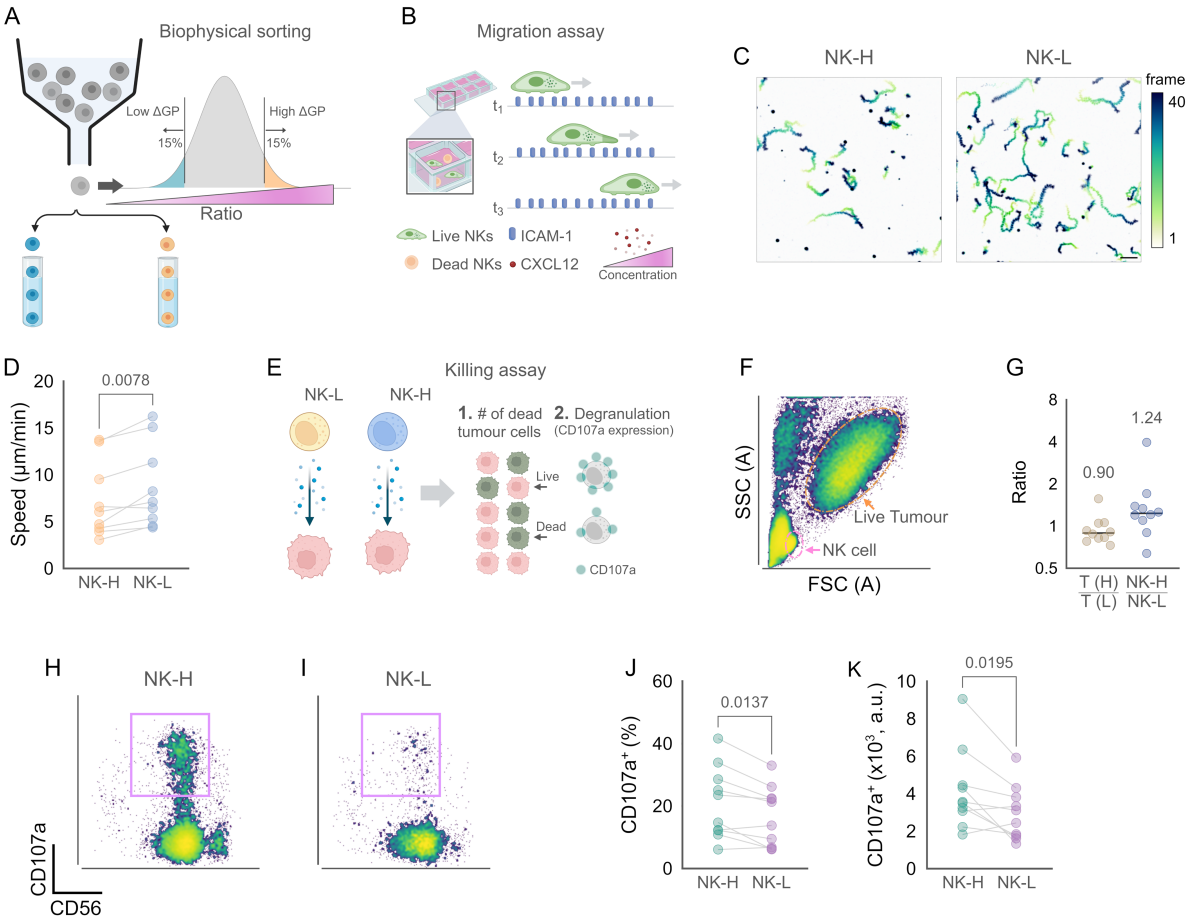

Figure 3. A) Schematic of the NK cell sorting based on their PM order. **B)** Schematic of the migration assay performed on NK-H and NK-L subsets. **C)** Example of migration trajectories recorded over a 40-frame period using confocal microscopy for the two NK cell subsets. **D)** Mean migration speed of the two NK cell subsets from individual donors (n = 9). **E)** Schematic of the killing assay performed on NK-H and NK-L subsets. **F)** Forward versus side scatter plot from flow cytometry analysis of NK cells after incubation with K562 tumour cells. **G)** Ratios between cell numbers of live tumour cells and NK cells from the low PM order-fraction (L) and high PM order-fraction (H), from individual donors after incubation with K562 tumour cells. The numbers refer to the mean ratio value. **H-I)** CD107a versus CD56 intensity plots from flow cytometry, showing the fraction of NK-H and NK-L cells that underwent degranulation upon incubation with K562 tumour cells. **J-K)** Percentage (J) of CD107a-expressing NK cells and mean CD107a intensity (K) in the two NK cell subsets from different donors. Statistical analysis in D, J and K plots was performed via Wilcoxon matched-pairs signed rank test.

Higher PM order in NK cells is associated with reduced immunosuppression. When we analysed the transcriptome of NK-L and NK-H, 261 genes were significantly downregulated in NK-H compared to NK-L cells, while only 37 genes were significantly upregulated (Fig. 4A and Fig. S14). The most significantly upregulated genes including RND1, NEU1, DHCR7, ZNF503-AS1 and SLC25A4, may play a role in cellular stress response and membrane dynamics[54–57]. On the other hand, the most significantly downregulated genes–MYBL2, TYMS, STMN1 and TK1–are associated with cell cycle regulation and proliferation[58–62]. Gene Ontology (GO) annotation using Gene Set Enrichment Analysis (GSEA), revealed a significant enrichment of downregulated genes that were localized to the external plasma membrane and the membrane of secretory granules (Fig. 4B). In terms of molecular function, NK-L cells showed significant downregulation of genes in pathways associated with immune receptor activity,

particularly cytokine receptors (Fig. 4C). In the biological process domain, significantly downregulated transcripts were enriched in pathways involved in cell cycle regulation, interleukin production, cytokine signalling, and chemotaxis (Fig. 4D).

Based on these pathway-level changes, we further examined individual genes that were significantly different between NK-H and NK-L cells. We first analysed whether the differences in membrane order would affect the expression of activating or inhibitory surface receptors. This is relevant because NK cell cytotoxicity against K562 tumour targets is mediated by receptor–ligand interactions, involving, for instance, NKG2D overexpression on NK cells[63] or upregulation of DNAM-1 ligands or TRAIL receptors (DR4/DR5) on K562 cells[64,65]. Although some genes related to receptor-mediated cytotoxicity were differentially expressed, the differences between NK-H and NK-L subsets were not statistically significant (Supplementary File on genes list). Interestingly, several differentially regulated genes were enriched in the Transforming Growth Factor-beta (TGF-β) signalling pathway from KEGG (Fig. S15). TGF-β is a multifunctional cytokine and a key mediator of immunosuppression[66]. In NK cells, TGF-β promotes the conversion of cytotoxic NK cells into less cytolytic ILC1-like cells[67], inhibits activation and cytotoxicity via repression of the mTOR pathway[68], reduces IFN-γ production, and downregulates activating receptors such as NKG2D and NKp30[67]. A recent study demonstrated that knockout of SMAD4, a downstream mediator of TGF-β signalling, preserves NK cell cytotoxicity[69]. In our transcriptomic analysis, we identified four genes that were significantly upregulated in NK-H cells compared to those with lower membrane order (Fig. 4E): BAMBI and TGIF1, both negative regulators of TGF-β signalling[70,71], and CITED2 and ID1, which are context-dependent modulators of TGF- β[72–77]. These findings suggest that the enhanced killing capacity of NK-H cells is linked to a functional inhibition of the crucial pathways including TGF-β pathway.

NK cells with lower PM order exhibit a more proliferative but less cytotoxic phenotype. While NK cells with increased PM order show indications of reduced TGF-β-dependent signalling, the NK-L subset displayed a genetic signature suggestive of increased proliferative potential. For example, NK-L cells showed significant upregulation of genes encoding Cyclin-dependent kinase 1 (CDK1) and Cell Division Cycle 25C (CDC25C, Fig. 4F). Their gene products regulate the transition from late G2 phase into mitosis and are mechanistically interconnected promoting a more proliferative state[78]. Given the enhanced proliferative phenotype, we tested whether NK-L cells might be undergoing a form of replication-induced exhaustion. However, our transcriptomic analysis did not reveal significant changes in the expression of exhaustion-associated inhibitory markers such as TIGIT, LAG-3, KLRC1, and PDCD1[79], nor in activating markers such as FCGR3A (CD16a) and KLRK1 (NKG2D)[80]. Conversely, NK-L cells showed significantly increased expression of BACH2 and BIRC5 (Survivin, Fig. 4F). BACH2 is a transcription factor and intrinsic negative regulator of NK cell maturation and cytotoxicity, typically overexpressed in immature CD56bright NK cells. Its regulation has been linked to Granzyme B (GzmB) production[81]. Similarly, BIRC5, commonly upregulated in proliferating cells[82], has been associated with reduced levels of intracellular cytotoxic proteins such as perforin, GzmB, TNF-α, and IFN-γ[83]. In addition, NK-L cells significantly overexpressed CCR7 and CD36 (Fig. 4G). CCR7 facilitates migration through recognition of its ligand CXCL12—used in our migration assay—and activation of the MAPK signalling pathway[84]. CD36, a master regulator of fatty acid uptake, promotes intracellular lipid accumulation[85]. Impaired lipid metabolism in CD36-overexpressing NK cells has been shown to reduce both cytotoxicity and migratory capacity[86–88]. Therefore, upregulation of CCR7 and CD36 may contribute to the enhanced migration observed in NK-L cells.

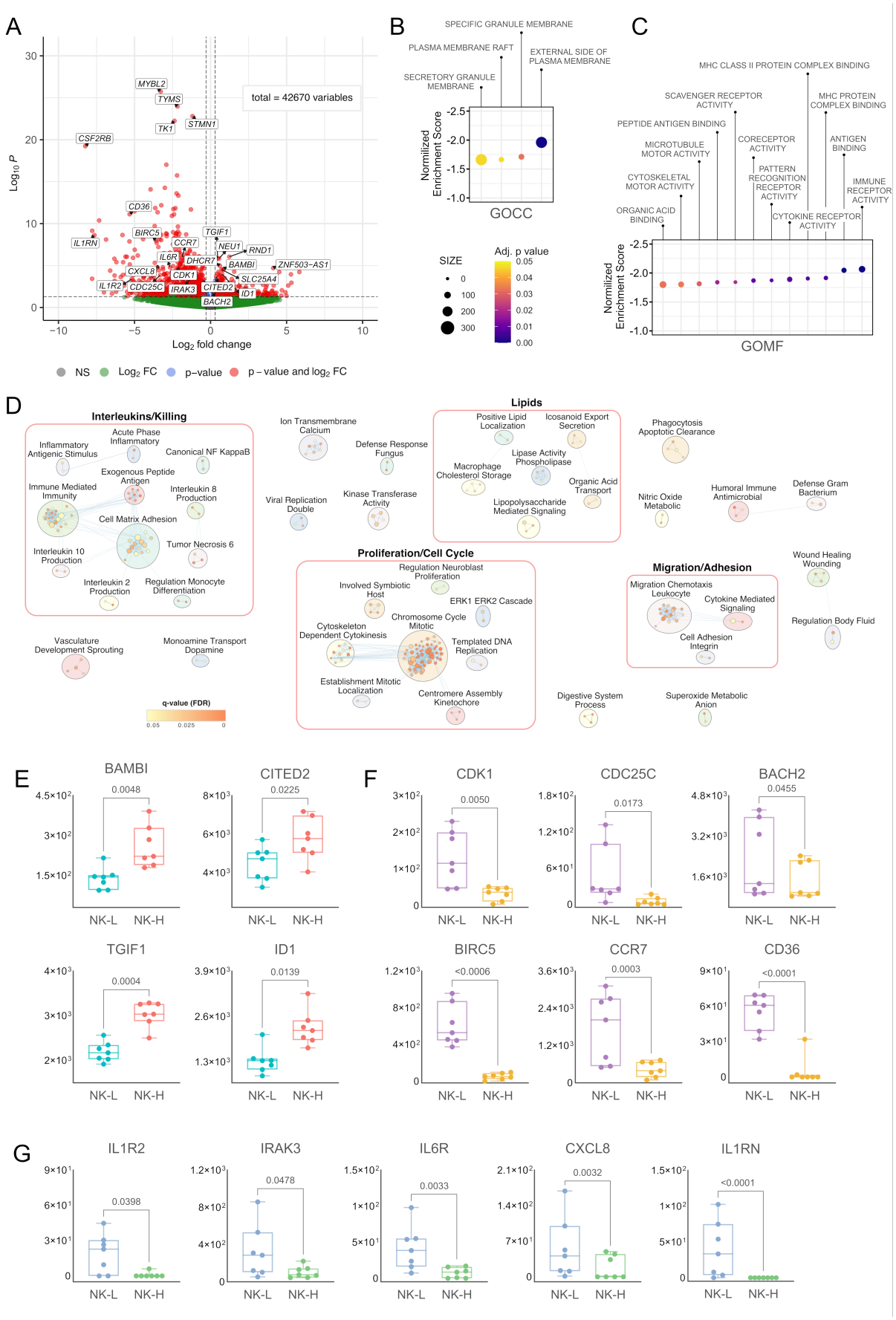

Figure 4. A) Volcano plots showing the genes differential expression in the NK-H subset compared to NK-L. **B-D)** Results from Gene Ontology (GO) annotation within the Cellular Components (**B**), Molecular Functions (**C**) and

Biological Processes (**D**) domains. **E-G)** Comparison of normalized gene counts between NK-L and NK-H subsets for selected genes. In panel B and C, the adj. p-values, are calculated using a permutation-based approach followed by correction for multiple comparisons using the false discovery rate (FDR) method, while in panels A, E-G the adjusted p-values are calculated using a generalized linear model (GLM) and corrected for multiple comparison using the Benjamini-Hochberg (BH) method.

NK cells with higher PM order show an interleukins-dependent pro-inflammatory phenotype. Notably, the NK-H subset showed a significant downregulation of several genes associated with interleukins (Fig. 4H). For instance, we observed transcriptional downregulation of CXCL8 (IL-8) and IL6R. The latter encodes for the Interleukin-6 (IL-6) receptor, and IL-6 has been shown to downregulate cytotoxicity of NK cells via reduction of perforin and granzyme B levels[89]. Remarkably, the NK-H subset showed significant downregulation of three different genes–IL1R2, IL1RN and IRAK3–which are involved in the regulation of the Interleukin-1 (IL-1) signalling pathway. Downregulation of IL1R2, IL1RN and IRAK3 indicate that NK cells with higher PM order might represent a subset of cells more sensitive to IL-1-mediated inflammation.

Discussion

Remodelling of the biophysical properties of immune cells—such as PM order—supports survival and optimal function in response to environmental changes. Here, we describe a novel pipeline for measuring PM order that combines environment-sensitive solvatochromic probes with the high-throughput, single-cell, multi-parameter capabilities of flow cytometry applied on all major types of immune cells in PBMCs simultaneously. Using this approach, we provide the first comprehensive characterization of PM order heterogeneity across peripheral blood immune cells and link alterations in this biophysical parameter to functional cell states in health and disease. Specifically, we analysed immune cells from healthy donors, patients with chronic lymphocytic leukemia (CLL), and individuals with long COVID (LC). Our findings revealed a consistent increase in membrane rigidity across most immune cell types under chronic inflammatory conditions. This phenomenon may stem from the dysregulated lipid metabolism and dyslipidaemia characteristic of both diseases. While previous studies have reported systemic lipid imbalances in these contexts, our method retains single-cell resolution and enables parallel analysis of multiple immune subsets. This resolution allowed us to detect subtle, cell-type-specific differences in PM order remodelling, highlighting that immune cells exposed to the same systemic alterations may respond differently depending on their identity or state. Moreover, correlations between PM order and additional biomarkers suggest that this feature serves as an orthogonal readout capable of identifying transient cellular states. These findings underscore the importance of investigating PM order remodelling as a mechanism of immune cell adaptation. For example, changes in membrane order may enhance immune cell survival within the tumour microenvironment (TME), promote migration[12], or increase effector function. Indeed, PM order has been shown to influence the integrity of immune synapses[90] and thus may play a key role in regulating immune responsiveness. While PM order changes can arise from specific pathways—such as drug exposure or receptor stimulation—in tumour-infiltrating cells, they may also result from complex, converging signals, including mechanical stress (e.g., increased pressure or confinement) and metabolic alterations within the TME. Therefore, quantifying PM order offers a simple yet powerful method to detect pathological cellular states, providing diagnostic sensitivity without requiring deep mechanistic dissection. The study of PM order using solvatochromic probes offers new insights into inflammation driven by pathogens, metabolic dysfunction, or even dietary factors with biophysical consequences.

While changes in membrane order can reflect altered cellular adaptation, PM order itself may encode unique phenotypic information, potentially serving as a marker of specific immune

functions. Through independent functional and transcriptomic profiling of sorted NK cells, we demonstrate that PM order can be used to isolate subsets with enhanced cytotoxicity or migratory potential. Although after cell culture conditions, membrane order equalized in different pools in our experiments, the functional and transcriptional differences were preserved. Future efforts will focus on extending PM order-based sorting to identify functional subsets in other immune cell types.

Our flow cytometry-based pipeline is versatile, multiplexable, and compatible with standard commercial cytometers. It can also be extended to assess additional biophysical features—such as membrane viscosity or tension—using specialized organelle-targeted probes[91]. As interest grows in cell biophysics as a determinant of immune function and disease, this work establishes PM order as a novel, orthogonal parameter that complements classical molecular analyses and paves the way for integrating biophysical phenotyping into routine biomedical research and diagnostics.

Methods

Synthesis of BSLBs with different membrane order. Silica beads and lipid species (Cholesterol, 1,2-dioleoyl-sn-glycero-3-phosphocholine (DOPC), 1-palmitoyl-2-oleoyl-glycero-3-phosphocholine (POPC) and 1,2-dipalmitoyl-sn-glycero-3-phosphocholine (DPPC)) were purchased from Bangs Laboratories and Avanti Polar Lipids, respectively. Synthesis of BSLBs consisted of two steps: *i)* formation of liposomes with given PM order and *ii)* coating of silica beads with a specific liposome composition. *Formation of liposomes*. For each lipid species, 10 µL of lipid solution in Chloroform (25 mg/mL) was transferred to a 1.5 mL Eppendorf and dried out under a Nitrogen flow. Then, 1 mL of *ad-hoc* buffer (SLB buffer: 10 mM HEPES, 150 mM NaCl, pH=7.4) was added to hydrate the lipid layer for 5 minutes under vigorous vortexing, and the solution was sonicated for 10 minutes (tip sonication, power=3, duty cycle=40%) to yield ~30 nm-sized liposomes. *Coating of silica beads*. 5 µm-sized beads were washed 2x with SLB buffer, resuspended in 45 µL of liposomes solution and diluted to 500 µL final volume in SLB buffer. Complete coating of silica beads was achieved after 30 minutes in bath sonication, after which beads were washed 2x in SLB buffer to remove excess of liposomes and stored a +4 ˚C.

Optimising resolution for PM order measurements. In our study we used Pro12A to probe PM order (Fig. S1)[39] both in synthetic and biological membranes. We prepared BLSBs with either low (DPPC-Cholesterol 1:1 coated beads) or high (DOPC coated beads) membrane order and used them to identify the best PMT voltages in the blue and green channels of the flow cytometer (BD LSRFortessa). 50 µL of liposomes-coated beads was diluted into 500 µL of SLB buffer and stained with 1.5 µL of Pro12A under vortexing. Acquisition of flow data started after 1 minute from dye addition. From the theoretical map of ΔGPs *vs* amplification factors (Fig. S2), we selected two different areas of low and high intensity signals and performed a voltration in one channel while keeping the PMT in the other channel constant. By doing so, we were able to identify the optimal pair of PMT voltages which ensured the highest resolution (*i.e.*, largest ΔGP between low and high order membranes) and reproducibility of GP measurements. For each lipid composition, we prepared four independent batches of BSLBs and acquired ≥ $5x10^3$ beads per measurement to ensure statistical robustness.

Pro12A internalization and cytotoxicity. We assessed degree of internalization and cytotoxicity of Pro12A by acquiring images in spectral confocal microscopy (LSM780 Zeiss microscope) over time and at different concentrations. Dye was considered internalized and cytotoxic when signal from the intracellular environment became visible or blebbing of the plasma membrane started occurring, respectively (Fig. S3). Internalization of Pro12A was

studied using CEM/C1 cells which were cultured in RPMI-1640 medium supplemented with 10% foetal bovine serum (FBS, Sigma Aldrich) at 37 °C and 5% CO2. 8-wells ibidi chambers were precoated with BSA (3 mg/mL) for 30 minutes and 100 µL of CEM/C1 cells ($6x10^6$ cells/mL in Leibovizt (L-15) medium) were added to each well and topped up with additional 300 µL of fresh L-15 medium. To each well, 1 µL of Pro12A was added to a final concentration of either 0.25 µM or 2.25 µM, and t-stack images were acquired (10 images every 90 seconds). Cell-specific plasma membrane order was calculated using our previously released software[92].

Study Participants. The present study analysed PBMCs from 13 healthy donors, 13 Long COVID patients and 5 CLL patients. For healthy donors, cells were isolated either from anonymous Buffy Coats (7 donors) or blood samples (6 donors raging from ages 27 to 44 years). Long COVID patients were characterized with >12 weeks of objectively measurable organ damage/dysfunction following PCR-verified SARS-CoV-2 infection and not explained by the severity of acute COVID or treatments for the same. The analysis included 12 post-acute sequelae of COVID-19 (PASC) patients and 1 recovered PASC patients (PASC-R). Long COVID patients ranged from ages 35 to 64 years. Venous blood samples were collected at a single time point for each individual. Informed consent was obtained from all patients. The Swedish ethical permit is covered under Dnr 2021-03293. Samples from Chronic Lymphocytes Leukaemia (CLL) patients were collected after 3 months from the second dose of vaccination against COVID-19. Patients were in their early-stage untreated CLL.

PBMCs isolation. PBMCs were isolated either from Buffy Coat (healthy donors) or blood (Long COVID and CLL patients) following a different protocol, depending on the sample. healthy donors and CLL patients: 45 mL of buffy coat was diluted 1:1 with PBS into 2x50 mL Falcon tubes and properly mixed. 30 mL of diluted solution was transferred in 2 new Falcon tubes pre-filled with 15 mL of Ficoll, using gravity-driven flow to overlay the diluted blood onto Filcoll. The tubes were centrifuged at 400 g for 25 minutes (brake off). The fraction containing PBMCs was collected into 2 new Falcon tubes and washed 2x with 45 mL PBS. During the washing steps, cells were pelleted by spinning the tubes at 300 g for 5 minutes (brake on). After the last washing, cells were resuspended in 20 mL PBS, filtered through a cell strainer, and pelleted one last time at 200 g for 10 minutes. After removal of the supernatant, cells were resuspended at a density of 10^8 cells/mL in a solution for cryopreservation (in 90% FBS + 10% DMSO) and stored in 1 mL batches at -140 ˚C until the analysis. *Long COVID patients:* Following plasma collection, blood was processed to isolate peripheral blood mononuclear cells (PBMCs) as follows: briefly, Lymphoprep™ (STEMCELL Technologies) was first added to SepMateTM tubes (STEMCELL Technologies) by carefully pipetting through the central hole of the SepMate insert, after which pre-diluted blood (Blood mixed with PBS + 2% FBS 1:1) was layered on the top of Lymphoprep™ (1 part of Lymphoprep : 2 parts of diluted blood) by pipetting it down the side of the tube carefully by minimizing the mixing of blood with Lymphoprep™ and centrifuged at 1200 x g for 10 minutes at ambient temperature (15 - 25°C) with the brake on. The top layer containing the enriched mononuclear cells (MNCs) was poured off into a new 50 mL tube and washed twice with PBS+2% FBS by centrifuging at 300 x g for 8 minutes at ambient temperature, with the brake on. Cells were then counted and cryopreserved (in 90% FBS + 10% DMSO) at a concentration of 5 million PBMCs/ml per cryotube stored at -80 ˚C first followed by transferring them to a liquid nitrogen tank for long-term storage.

Immune staining. Frozen PBMCs were thawed by adding a 10-fold volume of RPMI-1640 (Sigma-Aldrich) supplemented with 10% FBS (Sigma-Aldrich) and Benzonase Nuclease (10 units/mL, Sigma-Aldrich), pelleted at 400 g for 8 minutes, resuspended in 5 mL medium and allowed to recover. Since previous studies have shown that post-thaw resting of PBMCs may

or may not be beneficial depending on the cell type[93], we assessed the effect of different resting times after thawing on the PM order of major immune cell populations and compared the results with freshly isolated PBMCs analysed immediately after isolation (Fig. S16). On average, we observed a 6–12% decrease in PM order following freeze–thawing, with no significant differences between 1, 4, or 8 hours of recovery. However, prolonged incubation in culture medium led to an increase in apoptotic cells, particularly among monocyte-derived dendritic cells. Based on these findings, we opted for a minimum 1-hour recovery period—sufficient to restore membrane biophysical properties while minimizing apoptosis and ensure complete recovery of Monocytes and Dendritic cells. After recovery, PBMCs were pelleted at 400 g for 6 minutes and resuspended in Staining Buffer (eBioscience, ThermoFisher) at a concentration of $3x10^6$ cells/mL. Aliquots of 200 µL (*i.e.*, $6x10^5$ cells) in 0.5 mL Eppendorf were used to prepare single stained controls and multi-colour samples for flow cytometry. Optimal volumes of antibodies were obtained from calculation of staining indexes, and each aliquot was stained with either single antibody (for single stained controls) or a cocktail of antibodies. For panels containing more than one Brilliant Violet (BV) dye, 30 µL of Brilliant Stain Buffer (ThermoFisher) was added to prevent dye aggregation. Cells were incubated at 4 ˚C in the darkness for 30 minutes, washed 2x with PBS (Gibco™, pH 7.4) and resuspended in 300 µL. Then, cells were stained with 1 µL of Fixable Viability Stain 660 (BD Bioscience, stock solution: 5 ng/µL in DMSO) at room temperature for 15 minutes, washed 2x in PBS and resuspended to a final volume of 400 µL in the flow tubes. For each experiment, we built a different panel of fluorescent markers to gate on cells subpopulations, which was compatible with our probe for PM order, namely Pro12A. *Panel for PBMCs from healthy donors and patients*: PBMCs were stained with anti-Human CD45-FITC (clone HI30, BioLegend), CD3-BV605 (clone SK7, BD Biosciences), CD8-PE-FIRE700 (clone SK1, BioLegend), CD14-BV711 (clone M5E2, BioLegend), CD19-PE-Cy7 (clone SJ25C1, BioLegend), CD56-APC-R700 (clone NCAM16.2, BD Biosciences), CD11c-PE (clone Bu15, BioLegend). *Panel for NK sorting and killing assay:* Enriched NK cells were stained with CD3-PerCP-Cy5.5 (clone SK7, BioLegend), CD14-APC (clone M5E2, BioLegend), CD56-APC-R700 and FVS570 for cell viability. After incubation with K562 tumour cells, sorted NK cells were stained with CD56-PE (clone HCD56, BioLegend), CD3-PerCP-Cy5.5, CD107a-Alexa Fluor647 (clone H4A3, BD Biosciences) and FVS780 for cell viability. *Panel for apoptosis study:* PBMCs from healthy donors were stained with CD3-PerCP-Cy5.5, CD56-PE, CD19-PE-Cy7, Annexin-V-Alexa Fluor647 and FVS780 for cell viability. *Panel for assessing the effect of freezing-thawing on PM order:* PBMCs from healthy donors were stained with CD3-PerCP-Cy5.5, CD56-PE, CD19-PE-Cy7, CD11c-APC-R700 (clone 3.9, BD Biosciences), CD14-Alexa Fluor647 (clone M5E2, BioLegend), CD8-BV605 (clone SK1, BD Biosciences), Lactadherin-FITC (Prolitix) and FVS780 for cell viability. **Note:** Pro12A is generally measured using the BV4212 and BV510 channels. Therefore, depending on the flow cytometer configuration, some commercial fluorochromes might not be suitable for coupling with Pro12A given their spectral spillover. In our flow cytometry setup (Fig. S17), the following dyes are not compatible with PM order measurement via Pro12A: BUV395, BUV496, BV421, BV480, BV510, AlexaFluor405. The fluorochromes BUV563 and BV570 might require additional optimization and spillover assessment given the spectral proximity with Pro12A detection channels. On the other hand, the following fluorochromes can be safely coupled with Pro12A for PM order measurement: BUV615, BUV661, BUV737, BUV805, BV605, BV650, BV711, BV786. In addition, Pro12A can be coupled with all fluorochromes from the PE and PerCP family as well as the other AlexaFluor derivatives and the red-excitable dyes.

Analysis of PM order. After antibodies incubation, cells (400 µL at a concentration = $1.5x10^6$ cells/mL) were stained with 1.5 µL of Pro12A (100 µM in DMSO) and vortexed vigorously. After 1 minute from staining, we acquired flow data for ~5 minutes using a either a BD LSRFortessa 16-colour or a FACSCanto II flow cytometer. Before each experiment, we calibrated our flow

pipeline by running DOPC-coated beads stained with Pro12A and adjusting the PMT voltages of the blue and green channels so to ensure the same median GP value for DOPC beads. Data from flow were analysed in FCS Express (DeNovo Software) and GP values from individual cells were normalized to the GP_{DOPC} to remove day-to-day variability. Specifically, before starting analysis on cells, we always ran freshly made BSLBs coated with DOPC membrane and measured their median GP value. This value was systematically subtracted from the GP value of individual cells to yield a normalised PM order value.

NK cells sorting based on PM order. Before sorting, NK cells were enriched from PBMCs. Specifically, primary human NK cells were isolated by negative magnetic selection according to manufacturer protocol using a MojoSort human NK cell isolation kit (480054; BioLegend). The purity of enriched cells was >90%. Cells were counted (BioRad TC20) and checked for viability using trypan blue staining. After pre-enrichment, NK cells were stained with the antibodies cocktail (see above) and sorted based on their PM order. Cell sorting was performed on a BD FACSAria™ Fusion Flow Cytometer (BD Biosciences) equipped with 5 lasers, utilizing an 85 µm nozzle and running on FACS DIVA software. PM order was assessed by calculating the ratio between the intensities measured in the DAPI (ex. 405 nm, em. 450/50 nm) and the AmCyan (ex. 405 nm, em. 525/50 nm) channels. The DAPI/AmCyan ratio parameter was defined and created in the FACS DIVA software, and it was used as a regular fluorescence parameter thereafter. NK cell with high and low PM order were gated from the distribution of the DAPI/AMCyan ratios–as those falling below the 15th-percentile or above the 85th-percentile of the distribution–and collected in two falcon tubes. A small fraction of sorted cells was re-run both at the beginning and the end of the sorting procedure for purity check. Prior to sample analysis and sorting the instrument was calibrated with the BD® CS&T standard beads according to manufacturer's instructions for optimal operation. Throughout the sorting, the sample tube's temperature was kept at 20 °C to avoid changes in the cells' membrane order. Sorted cells were kept on ice until plated in culture medium for functional assays or processed for RNA extraction.

Migration assays on sorted NK cells. Migration assays were performed on agarose support. The protocol was adapted from a previously described method[94]. Briefly, 8-well polymer µ-slides (ibidi, 80821) were coated with recombinant human ICAM-1-Human-Fc chimera (RnD, 790-IC) at 3 µg/mL in PBS overnight at 4 °C. Slides were washed 3x with PBS, blocked with 2% bovine serum albumin (BSA) (Sigma-Aldrich) in PBS, and re-washed 3x. Agarose (0.5%, UltraPure Agarose, ThermoFisher) in RPMI+10% FCS-equivalent medium was prepared at 50 °C, and human CXCL12 (250 ng/mL RnD, 350-NS-010/CF) was added. 300 µL of agarose mixture was immediately pipetted in each µ-slide well. The agarose was placed at 4 °C for 1 h, and then transferred to 37 °C and 5% CO_2 for 30 min. ΔGP-sorted NK cells were rested overnight at 37 °C and 5% CO_2. The next day, cells were stained with CellTrace Violet (CTV, 1 µM, ThermoFisher) according to the manufacturer's instructions. Cells were resuspended in >10 µL of RPMI+10% FCS containing propidium iodide (1.5 µM) and injected under agarose with a pipette. Cells were acclimatized at the microscope for at least 30 min at 37 °C and subsequently imaged every 15 s for 10 min using a Zeiss LSM780. Images were acquired with a Zeiss 20x (0.75 NA) objective, at 512 × 512 resolution in 8-bit using Zeiss Zen. Cells were tracked using the FIJI plugin TrackMate[95]. Propidium iodide-positive dead cells and tracks shorter than half the video length were excluded from analysis.

Killing assays on sorted NK cells. The killing capacity of NK-H and NK-L cells was assessed via degranulation assay as previously described[96]. Briefly, sorted NK cells were resuspended in complete PRMI medium ($1{,}2 \times 10^6$ live cells/mL), transferred in a V-bottom 96-well plates and co-cultured with K562 cells (ATCC) at 1:1 effector-to-target ratio in the presence of mouse anti-human CD107a Alexa Fluor 647 (BD Bioscience, clone H4A3, 2 µL/well) for 6 hours at

37°C. To block intracellular protein transport, BD GolgiStop (BD Bioscience) was added at a final concentration of 1:1000 during the assay after 1 hour of incubation. Once the 6 hours of incubation were completed, cells were washed twice in PBS + 2% FBS and stained with a cocktail of antibodies as described above for 30 minutes at 4°C in the dark, followed by two washes in PBS and staining with fixable Viability Stain (final concentration 1:1000) for 15 minutes at room temperature. Stained cells were washed in PBS once, stained with Pro12A and analysed in flow cytometry.

UMAP analysis for clusters identification. Dimensionality reduction analysis was performed on live-CD45^{+}-gated cells using FCS express software. All fluorescent parameters (except ΔGP) were scaled using a biexponential transformation setting the Below Zero parameter equal to 800. ΔGP values were scaled following a linear method. Cells were down sampled to ~4x10^{5} cells following a random down-sampling method. For UMAP analysis, we set number of neighbours equal to 50, Min Low Distance equal to 0.4 and number of iterations equal to 600.

RNA extraction and transcriptomic analysis. For the RNA extraction, a fraction of sorted NK cells was washed with 1X-PBS buffer 3 times, re-suspended in 1 mL TRIzol™ Reagent (15596018; ThermoFisher), and stored at -80°C until isolation. Organic extraction method was applied with chloroform addition and isopropanol precipitation. RNA Clean & Concentrator-5 (Zymo Research) was used for further purification and concentration.

Library preparation and sequencing were performed at the Bioinformatics and Expression Analysis (BEA) core facility at Karolinska Institutet. All libraries were prepared using Takara's SMART-SEQ V4 protocol and sequenced on a Nextseq 2000 sequencer with a P2 100 cycle flow cell. Cycling parameters were: 61 * 61 cycles paired end run with 8 cycles dual index. Base-calling and demultiplexing was performed using bcl2fastq (v2.20.0.422). Subsequently, quality control of the read sequences was performed with FastQC (v0.12.0, https://www.bioinformatics.babraham.ac.uk/projects/fastqc/), followed by preparation for alignment using CutAdapt (v3.5, adapter and quality trimming)[97]. Read alignment was completed with STAR aligner (v2.7.9a)[98], made to the reference genome GRCh38 and genomic features were assigned using featureCounts (v1.5.1)[99]. Differential gene expression (DGE) analysis was performed with the DESeq2 package (v1.46.0)[100] in R (v4.4.3)[101], with the linear model design = ~ Batch + GP_Status. The significance thresholds used were adjusted p value<0.05 (Benjamini-Hochberg adjustment), base mean>20 and absolute log2 fold change>0.3. For easy visualisation, principal component analysis (PCA) was performed using the pcaExplorer package (v3.0.0)[102] in R (v4.4.3)[101]. Included heatmaps and plots were prepared using the pheatmap (v1.0.12, https://cran.r-project.org/package=pheatmap) and ggplot2 (v3.5.1) packages[103] in R (v4.4.3)[101].

Pathway analysis was performed as per a previously described protocol[104]. After the DGE analysis, RNK files were created and Gene-Set Enrichment Analysis (GSEA, v4.4.0)[105] was performed for biological process (MSigDB v2024.1), molecular function (MSigDB v2024.1), and cellular component (MSigDB v2024.1), with a significance threshold cutoff of FDR<0.05. The scored gene ontology information for biological process was imported into Cytoscape (v3.10.3)[106] and visualized using the EnrichmentMap (v3.5.0)[107] app. The generated clusters with FDR adjusted p values (q values) were subsequently labelled using the AutoAnnotate (v1.5.2)[108] app, to identify enriched pathways, that were differentially regulated. GSEA was also performed for KEGG pathways[109] using the clusterProfiler package (v4.14.6)[110] in R(v4.4.3)[101]. The enrichment of differentially expressed genes was also visualised in selected KEGG pathways[109] using the pathview package (v1.46.0)[111] in R (v4.4.3).

Data availability

All data in this manuscript will be publicly available at FigShare repository upon publication.

Code availability

Analysis of PM order from confocal microscopy images was performed our recently published open-source software VISION[92].

Acknowledgments

This work is supported by Swedish Research Council Grants (grant no. 2020-02682, 2024-02993 and 2024-00289), Wellcome Leap's Dynamic Resilience Program (jointly funded by Temasek Trust), Karolinska Institutet (2024-03250; 2024-03341; 2022-00803; 2020-00997), Cancer Research KI (2024-03488), SciLifeLab, Human Frontier Science Program (RGP0025/2022), Longevity Impetus Grant from Norn Group, Hevolution Foundation and Rosenkranz Foundation. We thank the SciLifeLab Advanced Light Microscopy facility and National Microscopy Infrastructure (VR-RFI 2016-00968) for their support on imaging. We also thank the core facility Bioinformatics and Expression Analysis (BEA) at NEO for their support with RNA extraction and analysis.

Author contributions

L.A, E.S conceived and designed the experiments. L.A performed all the experiments together with Y.J and S.I (for experiment on PMBCs isolated from donors), P.S and V.C (for experiments on NK cells), L.B for experiments on NK cells migration, C.G and S.G for experiments on NK cells sorting, and A.A for transcriptomic analysis. J.M and P.B. helped with collection of samples from long COVID patients and provide scientific insights. M.B and A.Ö helped with collection of samples from CLL patients and provided scientific insights. P.S provided scientific insights on NK cells killing assays. B.Ö provided scientific insights on NK cells. A.S.K. provided Pro12A and insights on its use. L.A and E.S co-wrote the manuscript. All authors read and corrected the manuscript.

Competing interests

Authors declare no completing interest.

References

1. Combes, A. J., Samad, B. & Krummel, M. F. Defining and using immune archetypes to classify and treat cancer. *Nat. Rev. Cancer* **23**, 491–505 (2023).
2. Mujal, A. M. & Krummel, M. F. Immunity as a continuum of archetypes. *Science* **364**, 28–29 (2019).
3. Lareau, C. Subtle cell states resolved in single-cell data. *Nat. Biotechnol.* 1–2 (2023) doi:10.1038/s41587-023-01797-6.
4. Olzmann, J. A. & Carvalho, P. Dynamics and functions of lipid droplets. *Nat. Rev. Mol. Cell Biol.* **20**, 137–155 (2019).
5. Alberts, B. *et al.* The Lipid Bilayer. in *Molecular Biology of the Cell. 4th edition* (Garland Science, 2002).

6. Casares, D., Escribá, P. V. & Rosselló, C. A. Membrane Lipid Composition: Effect on Membrane and Organelle Structure, Function and Compartmentalization and Therapeutic Avenues. *Int. J. Mol. Sci.* **20**, 2167 (2019).
7. Wymann, M. P. & Schneiter, R. Lipid signalling in disease. *Nat. Rev. Mol. Cell Biol.* **9**, 162–176 (2008).
8. Wilson, K. A., MacDermott-Opeskin, H. I., Riley, E., Lin, Y. & O'Mara, M. L. Understanding the Link between Lipid Diversity and the Biophysical Properties of the Neuronal Plasma Membrane. *Biochemistry* **59**, 3010–3018 (2020).
9. Lorent, J. H. *et al.* Plasma membranes are asymmetric in lipid unsaturation, packing and protein shape. *Nat. Chem. Biol.* **16**, 644–652 (2020).
10. Atilla-Gokcumen, G. E. *et al.* Dividing Cells Regulate Their Lipid Composition and Localization. *Cell* **156**, 428–439 (2014).
11. Kunduri, G., Acharya, U. & Acharya, J. K. Lipid Polarization during Cytokinesis. *Cells* **11**, 3977 (2022).
12. Braig, S. *et al.* Pharmacological targeting of membrane rigidity: implications on cancer cell migration and invasion. *New J. Phys.* **17**, 083007 (2015).
13. Edmond, V. *et al.* Downregulation of ceramide synthase-6 during epithelial-to-mesenchymal transition reduces plasma membrane fluidity and cancer cell motility. *Oncogene* **34**, 996–1005 (2015).
14. Zhao, W. *et al.* Candidate Antimetastasis Drugs Suppress the Metastatic Capacity of Breast Cancer Cells by Reducing Membrane Fluidity. *Cancer Res.* **76**, 2037–2049 (2016).
15. Lühr, J. J. *et al.* Maturation of Monocyte-Derived DCs Leads to Increased Cellular Stiffness, Higher Membrane Fluidity, and Changed Lipid Composition. *Front. Immunol.* **11**, 590121 (2020).
16. Matias, M. I. *et al.* Regulatory T cell differentiation is controlled by αKG-induced alterations in mitochondrial metabolism and lipid homeostasis. *Cell Rep.* **37**, 109911 (2021).
17. Owen, D. M. *et al.* High plasma membrane lipid order imaged at the immunological synapse periphery in live T cells. *Mol. Membr. Biol.* **27**, 178–189 (2010).
18. Rentero, C. *et al.* Functional Implications of Plasma Membrane Condensation for T Cell Activation. *PLOS ONE* **3**, e2262 (2008).
19. Urbančič, I. *et al.* Aggregation and mobility of membrane proteins interplay with local lipid order in the plasma membrane of T cells. *FEBS Lett.* **595**, 2127–2146 (2021).
20. Tello-Lafoz, M. *et al.* Cytotoxic lymphocytes target characteristic biophysical vulnerabilities in cancer. *Immunity* **54**, 1037-1054.e7 (2021).
21. Rudd-Schmidt, J. A. *et al.* Lipid order and charge protect killer T cells from accidental death. *Nat. Commun.* **10**, 5396 (2019).
22. Li, Y. & Orange, J. S. Degranulation enhances presynaptic membrane packing, which protects NK cells from perforin-mediated autolysis. *PLOS Biol.* **19**, e3001328 (2021).
23. Benninger, R. K. P. *et al.* Live Cell Linear Dichroism Imaging Reveals Extensive Membrane Ruffling within the Docking Structure of Natural Killer Cell Immune Synapses. *Biophys. J.* **96**, L13 (2009).
24. Pollock, A. H. *et al.* Prolonged Intake of Dietary Lipids Alters Membrane Structure and T Cell Responses in LDLr−/− Mice. *J. Immunol.* **196**, 3993–4002 (2016).
25. Zani, F. *et al.* The dietary sweetener sucralose is a negative modulator of T cell-mediated responses. *Nature* **615**, 705–711 (2023).
26. Niko, Y. & Klymchenko, A. S. Emerging solvatochromic push–pull dyes for monitoring the lipid order of biomembranes in live cells. *J. Biochem. (Tokyo)* **170**, 163–174 (2021).
27. Ragaller, F. *et al.* Dissecting the mechanisms of environment sensitivity of smart probes for quantitative assessment of membrane properties. *Open Biol.* **12**, 220175.

28. Amaro, M., Reina, F., Hof, M., Eggeling, C. & Sezgin, E. Laurdan and Di-4-ANEPPDHQ probe different properties of the membrane. *J. Phys. D* **50**, 134004 (2017).
29. Klymchenko, A. S. Fluorescent Probes for Lipid Membranes: From the Cell Surface to Organelles. *Acc. Chem. Res.* **56**, 1–12 (2023).
30. García-Calvo, J. *et al.* HydroFlipper membrane tension probes: imaging membrane hydration and mechanical compression simultaneously in living cells. *Chem. Sci.* **13**, 2086–2093 (2022).
31. Ragaller, F. *et al.* Quantifying Fluorescence Lifetime Responsiveness of Environment-Sensitive Probes for Membrane Fluidity Measurements. *J. Phys. Chem. B* **128**, 2154–2167 (2024).
32. Klymchenko, A. S. Solvatochromic and Fluorogenic Dyes as Environment-Sensitive Probes: Design and Biological Applications. *Acc. Chem. Res.* **50**, 366–375 (2017).
33. Danylchuk, D. I., Moon, S., Xu, K. & Klymchenko, A. S. Switchable Solvatochromic Probes for Live-Cell Super-resolution Imaging of Plasma Membrane Organization. *Angew. Chem. Int. Ed.* **58**, 14920–14924 (2019).
34. Darwich, Z., Klymchenko, A. S., Kucherak, O. A., Richert, L. & Mély, Y. Detection of apoptosis through the lipid order of the outer plasma membrane leaflet. *Biochim. Biophys. Acta* **1818**, 3048–3054 (2012).
35. Marielle, B. & Sarrah, G. Assessment of bacterial membrane fluidity by flow cytometry. *J. Microbiol. Methods* **143**, 50–57 (2017).
36. Kaiser, H.-J. *et al.* Molecular convergence of bacterial and eukaryotic surface order. *J. Biol. Chem.* **286**, 40631–40637 (2011).
37. Weiss, L., Bonnet, D., Dziuba, D. & Karpenko, J. Flow Cytometry Analysis of Perturbations in the Bacterial Cell Envelope Enabled by Monitoring Generalized Polarization of the Solvatochromic Peptide UNR-1. *Anal. Chem.* **97**, 622–628 (2025).
38. Miguel, L. *et al.* Primary Human CD4+ T Cells Have Diverse Levels of Membrane Lipid Order That Correlate with Their Function. *J. Immunol.* **186**, 3505–3516 (2011).
39. Danylchuk, D. I., Sezgin, E., Chabert, P. & Klymchenko, A. S. Redesigning Solvatochromic Probe Laurdan for Imaging Lipid Order Selectively in Cell Plasma Membranes. *Anal. Chem.* **92**, 14798–14805 (2020).
40. Carravilla, P. *et al.* Measuring plasma membrane fluidity using confocal microscopy. *Nat. Protoc.* (2025) doi:10.1038/s41596-024-01122-8.
41. Mohammed, R. N. *et al.* A comprehensive review about immune responses and exhaustion during coronavirus disease (COVID-19). *Cell Commun. Signal.* **20**, 79 (2022).
42. Virgin, H. W., Wherry, E. J. & Ahmed, R. Redefining Chronic Viral Infection. *Cell* **138**, 30–50 (2009).
43. Varchetta, S. & Marcenaro, E. Editorial: Innate and adaptive immune responses to viral infection. *Front. Virol.* **5**, (2025).
44. Schreiber, R. D., Old, L. J. & Smyth, M. J. Cancer Immunoediting: Integrating Immunity's Roles in Cancer Suppression and Promotion. *Science* **331**, 1565–1570 (2011).
45. Hiam-Galvez, K. J., Allen, B. M. & Spitzer, M. H. Systemic immunity in cancer. *Nat. Rev. Cancer* **21**, 345–359 (2021).
46. Roerden, M. & Spranger, S. Cancer immune evasion, immunoediting and intratumour heterogeneity. *Nat. Rev. Immunol.* 1–17 (2025) doi:10.1038/s41577-024-01111-8.
47. Santinho, A., Carpentier, M., Lopes Sampaio, J., Omrane, M. & Thiam, A. R. Giant organelle vesicles to uncover intracellular membrane mechanics and plasticity. *Nat. Commun.* **15**, 3767 (2024).
48. Zhang, Y., Chen, X., Gueydan, C. & Han, J. Plasma membrane changes during programmed cell deaths. *Cell Res.* **28**, 9–21 (2018).
49. Shlomovitz, I., Speir, M. & Gerlic, M. Flipping the dogma – phosphatidylserine in non-apoptotic cell death. *Cell Commun. Signal.* **17**, 139 (2019).

50. Sputay, D. *et al.* Immune cell activation produces locally scrambled foci of plasma membrane lipids. *Faraday Discuss.* (2025) doi:10.1039/D4FD00205A.
51. Kristenson, L. *et al.* Deletion of the TMEM30A gene enables leukemic cell evasion of NK cell cytotoxicity. *Proc. Natl. Acad. Sci.* **121**, e2316447121 (2024).
52. Doktorova, M. *et al.* Cell membranes sustain phospholipid imbalance via cholesterol asymmetry. *Cell* (2025) doi:10.1016/j.cell.2025.02.034.
53. Alter, G., Malenfant, J. M. & Altfeld, M. CD107a as a functional marker for the identification of natural killer cell activity. *J. Immunol. Methods* **294**, 15–22 (2004).
54. Wen, H. *et al.* Mitochondrial diseases: from molecular mechanisms to therapeutic advances. *Signal Transduct. Target. Ther.* **10**, 9 (2025).
55. Temple, S. E. L., Sachdev, R. & Ellaway, C. Familial DHCR7 genotype presenting as a very mild form of Smith-Lemli-Opitz syndrome and lethal holoprosencephaly. *JIMD Rep.* **56**, 3–8 (2020).
56. Du, J. *et al.* Neuraminidase-1 (NEU1): Biological Roles and Therapeutic Relevance in Human Disease. *Curr. Issues Mol. Biol.* **46**, 8031–8052 (2024).
57. Guo, Z. *et al.* NEU1 Regulates Mitochondrial Energy Metabolism and Oxidative Stress Post-myocardial Infarction in Mice via the SIRT1/PGC-1 Alpha Axis. *Front. Cardiovasc. Med.* **9**, (2022).
58. Musa, J., Aynaud, M.-M., Mirabeau, O., Delattre, O. & Grünewald, T. G. MYBL2 (B-Myb): a central regulator of cell proliferation, cell survival and differentiation involved in tumorigenesis. *Cell Death Dis.* **8**, e2895 (2017).
59. Song, S. *et al.* Diagnostic and prognostic value of thymidylate synthase expression in breast cancer. *Clin. Exp. Pharmacol. Physiol.* **48**, 279–287 (2021).
60. Lee, C.-J. *et al.* Thymidine Kinase 1 Expression Correlates with Tumor Aggressiveness and Metastatic Potential in OSCC. *Diagnostics* **15**, 1567 (2025).
61. Chen, Y.-L., Eriksson, S. & Chang, Z.-F. Regulation and Functional Contribution of Thymidine Kinase 1 in Repair of DNA Damage. *J. Biol. Chem.* **285**, 27327–27335 (2010).
62. Côrte-Real, B. F., Arroyo Hornero, R., Dyczko, A., Hamad, I. & Kleinewietfeld, M. Dissecting the role of CSF2RB expression in human regulatory T cells. *Front. Immunol.* **13**, (2022).
63. Epling-Burnette, P. K. *et al.* Reduced natural killer (NK) function associated with high-risk myelodysplastic syndrome (MDS) and reduced expression of activating NK receptors. *Blood* **109**, 4816–4824 (2007).
64. Kearney, C. J., Ramsbottom ,Kelly M., Voskoboinik ,Ilia, Darcy ,Phillip K. & and Oliaro, J. Loss of DNAM-1 ligand expression by acute myeloid leukemia cells renders them resistant to NK cell killing. *OncoImmunology* **5**, e1196308 (2016).
65. Liu, L., Hussain, S. A. & Hu, X. Fisetin reduces the resistance of MOLT-4 and K562 cells to TRAIL-induced apoptosis through upregulation of TRAIL receptors. *Naunyn. Schmiedebergs Arch. Pharmacol.* **397**, 9689–9700 (2024).
66. Deng, Z. *et al.* TGF-β signaling in health, disease and therapeutics. *Signal Transduct. Target. Ther.* **9**, 1–40 (2024).
67. Regis, S., Dondero, A., Caliendo, F., Bottino, C. & Castriconi, R. NK Cell Function Regulation by TGF-β-Induced Epigenetic Mechanisms. *Front. Immunol.* **11**, (2020).
68. Viel, S. *et al.* TGF-β inhibits the activation and functions of NK cells by repressing the mTOR pathway. *Sci. Signal.* **9**, ra19–ra19 (2016).
69. Rea, A. *et al.* Enhancing human NK cell antitumor function by knocking out SMAD4 to counteract TGFβ and activin A suppression. *Nat. Immunol.* **26**, 582–594 (2025).
70. Onichtchouk, D. *et al.* Silencing of TGF-β signalling by the pseudoreceptor BAMBI. *Nature* **401**, 480–485 (1999).

71. Sekiya, T., Oda, T., Matsuura, K. & Akiyama, T. Transcriptional regulation of the TGF-β pseudoreceptor BAMBI by TGF-β signaling. *Biochem. Biophys. Res. Commun.* **320**, 680–684 (2004).
72. Chou, Y.-T. & Yang, Y.-C. Post-transcriptional Control of Cited2 by Transforming Growth Factor β: REGULATION VIA SMADS AND CITED2 CODING REGION *. *J. Biol. Chem.* **281**, 18451–18462 (2006).
73. Chou, Y.-T., Wang, H., Chen, Y., Danielpour, D. & Yang, Y.-C. Cited2 modulates TGF-β-mediated upregulation of MMP9. *Oncogene* **25**, 5547–5560 (2006).
74. Chou, Y.-T. *et al.* CITED2 functions as a molecular switch of cytokine-induced proliferation and quiescence. *Cell Death Differ.* **19**, 2015–2028 (2012).
75. Liang, Y.-Y., Brunicardi, F. C. & Lin, X. Smad3 mediates immediate early induction of Id1 by TGF-β. *Cell Res.* **19**, 140–148 (2009).
76. Lin, L. *et al.* Cross talk between Id1 and its interactive protein Dril1 mediate fibroblast responses to transforming growth factor-beta in pulmonary fibrosis. *Am. J. Pathol.* **173**, 337–346 (2008).
77. Tang, B. *et al.* Transforming Growth Factor-β Can Suppress Tumorigenesis through Effects on the Putative Cancer Stem or Early Progenitor Cell and Committed Progeny in a Breast Cancer Xenograft Model. *Cancer Res.* **67**, 8643–8652 (2007).
78. Liu, K. *et al.* The role of CDC25C in cell cycle regulation and clinical cancer therapy: a systematic review. *Cancer Cell Int.* **20**, 213 (2020).
79. Judge, S. J., Murphy, W. J. & Canter, R. J. Characterizing the Dysfunctional NK Cell: Assessing the Clinical Relevance of Exhaustion, Anergy, and Senescence. *Front. Cell. Infect. Microbiol.* **10**, (2020).
80. Jin, Y. *et al.* NK Cell Exhaustion in Wilson's Disease Revealed by Single-cell RNA Sequencing Predicts the Prognosis of Cholecystitis. *eLife* **13**, (2024).
81. Imianowski, C. J. *et al.* BACH2 restricts NK cell maturation and function, limiting immunity to cancer metastasis. *J. Exp. Med.* **219**, e20211476 (2022).
82. Wheatley, S. P. & Altieri, D. C. Survivin at a glance. *J. Cell Sci.* **132**, jcs223826 (2019).
83. Ferguson Bennit, H. R. *et al.* Natural Killer Cell Phenotype and Functionality Affected by Exposure to Extracellular Survivin and Lymphoma-Derived Exosomes. *Int. J. Mol. Sci.* **22**, 1255 (2021).
84. Guyon, A. CXCL12 chemokine and its receptors as major players in the interactions between immune and nervous systems. *Front. Cell. Neurosci.* **8**, (2014).
85. Samovski, D., Jacome-Sosa, M. & Abumrad, N. A. Fatty Acid Transport and Signaling: Mechanisms and Physiological Implications. *Annu. Rev. Physiol.* **85**, 317–337 (2023).
86. Kobayashi, T. *et al.* Increased lipid metabolism impairs NK cell function and mediates adaptation to the lymphoma environment. *Blood* **136**, 3004–3017 (2020).
87. Niavarani, S. R. *et al.* Lipid accumulation impairs natural killer cell cytotoxicity and tumor control in the postoperative period. *BMC Cancer* **19**, 823 (2019).
88. Schimmer, S. *et al.* Fatty acids are crucial to fuel NK cells upon acute retrovirus infection. *Front. Immunol.* **14**, (2023).
89. Cifaldi, L. *et al.* Inhibition of Natural Killer Cell Cytotoxicity by Interleukin-6: Implications for the Pathogenesis of Macrophage Activation Syndrome. *Arthritis Rheumatol.* **67**, 3037–3046 (2015).
90. Jung, P., Zhou, X., Iden, S., Bischoff, M. & Qu, B. T cell stiffness is enhanced upon formation of immunological synapse. *eLife* **10**, e66643 (2021).
91. Paez-Perez, M. & Kuimova, M. K. Molecular Rotors: Fluorescent Sensors for Microviscosity and Conformation of Biomolecules. *Angew. Chem. Int. Ed.* **n/a**, e202311233.
92. Weber, F. *et al.* VISION – an open-source software for automated multi-dimensional image analysis of cellular biophysics. *J. Cell Sci.* **137**, jcs262166 (2024).

93. Wang, L. *et al.* Standardization of cryopreserved peripheral blood mononuclear cells through a resting process for clinical immunomonitoring—Development of an algorithm. *Cytometry A* **89**, 246–258 (2016).
94. de Boer, L. L. *et al.* T cell migration requires ion and water influx to regulate actin polymerization. *Nat. Commun.* **14**, 7844 (2023).
95. Tinevez, J.-Y. *et al.* TrackMate: An open and extensible platform for single-particle tracking. *Methods* **115**, 80–90 (2017).
96. Bryceson, Y. T. *et al.* Functional analysis of human NK cells by flow cytometry. *Methods Mol. Biol. Clifton NJ* **612**, 335–352 (2010).
97. Martin, M. Cutadapt removes adapter sequences from high-throughput sequencing reads. *EMBnet.journal* **17**, 10–12 (2011).
98. Dobin, A. *et al.* STAR: ultrafast universal RNA-seq aligner. *Bioinformatics* **29**, 15–21 (2013).
99. Liao, Y., Smyth, G. K. & Shi, W. featureCounts: an efficient general purpose program for assigning sequence reads to genomic features. *Bioinformatics* **30**, 923–930 (2014).
100. Love, M. I., Huber, W. & Anders, S. Moderated estimation of fold change and dispersion for RNA-seq data with DESeq2. *Genome Biol.* **15**, 550 (2014).
101. Dia, M., Wehner, T. C. & Arellano, C. RGxE: An R Program for Genotype x Environment Interaction Analysis. *Am. J. Plant Sci.* **08**, 1672–1698 (2017).
102. Marini, F. & Binder, H. pcaExplorer: an R/Bioconductor package for interacting with RNA-seq principal components. *BMC Bioinformatics* **20**, 331 (2019).
103. Wickham, H. *Ggplot2: Elegant Graphics for Data Analysis*. (Springer New York, New York, NY, 2009). doi:10.1007/978-0-387-98141-3.
104. Reimand, J. *et al.* Pathway enrichment analysis and visualization of omics data using g:Profiler, GSEA, Cytoscape and EnrichmentMap. *Nat. Protoc.* **14**, 482–517 (2019).
105. Gene set enrichment analysis: A knowledge-based approach for interpreting genome-wide expression profiles | PNAS. https://www.pnas.org/doi/10.1073/pnas.0506580102.
106. Shannon, P. *et al.* Cytoscape: a software environment for integrated models of biomolecular interaction networks. *Genome Res.* **13**, 2498–2504 (2003).
107. Merico, D., Isserlin, R., Stueker, O., Emili, A. & Bader, G. D. Enrichment map: a network-based method for gene-set enrichment visualization and interpretation. *PloS One* **5**, e13984 (2010).
108. Kucera, M., Isserlin, R., Arkhangorodsky, A. & Bader, G. D. AutoAnnotate: A Cytoscape app for summarizing networks with semantic annotations. *F1000Research* **5**, 1717 (2016).
109. Kanehisa, M., Furumichi, M., Sato, Y., Matsuura, Y. & Ishiguro-Watanabe, M. KEGG: biological systems database as a model of the real world. *Nucleic Acids Res.* **53**, D672–D677 (2025).
110. Wu, T. *et al.* clusterProfiler 4.0: A universal enrichment tool for interpreting omics data. *Innov. Camb. Mass* **2**, 100141 (2021).
111. Luo, W. & Brouwer, C. Pathview: an R/Bioconductor package for pathway-based data integration and visualization. *Bioinformatics* **29**, 1830–1831 (2013).